

# Non-linear Optimization Scheme Applied to EIT Medical Images Based on the Gauss-Newton Method With Iterative Conductivity Update and Total Variation Regularization

Bruno Miguel Gil Rosa (✉ [b.gil-rosa@imperial.ac.uk](mailto:b.gil-rosa@imperial.ac.uk))

Imperial College London

Guang-Zhong Yang

Shanghai Jiao Tong University

---

## Research Article

**Keywords:** Computerized Tomography (CT), Non-linear Optimization Scheme, EIT Medical Images, Gauss-Newton Method, Iterative Conductivity, Total Variation Regularization

**Posted Date:** June 3rd, 2021

**DOI:** <https://doi.org/10.21203/rs.3.rs-577632/v1>

**License:**  This work is licensed under a Creative Commons Attribution 4.0 International License.

[Read Full License](#)

---

# 1 Non-linear Optimization Scheme applied to EIT 2 Medical Images based on the Gauss-Newton Method 3 with Iterative Conductivity Update and Total 4 Variation Regularization

5 **Bruno Miguel Gil Rosa<sup>1,\*</sup> and Guang-Zhong Yang<sup>2</sup>**

6 <sup>1</sup>The Hamlyn Centre, Imperial College London, London, SW7 2AZ, United Kingdom

7 <sup>2</sup>Institute of Medical Robotics, Shanghai Jiao Tong University, Shanghai, 200240, China

8 \*b.gil-rosa@imperial.ac.uk

## 9 ABSTRACT

Medical imaging modalities are vast and include the well-established techniques of Computerized Tomography (CT), Magnetic Resonance Imaging (MRI) or Ultrasounds. Though the underlying physics differs amongst modalities, a similar Inverse Mapping is shared: the recovery of the internal physical property under analysis from measurements obtained at the exterior of the body. In the lesser common technique of Electrical Impedance Tomography (EIT), measurement of the voltage levels around a body part are used to retrieve the internal distribution map for conductivity. The complexity of the Inverse Problem in EIT surpasses that found for the Forward Problem (or Mapping), both in terms of mathematical formulation and computational overload. The ill-posed nature of the Inverse Problem further contributes to that intricacy, and solutions to tackle it will be presented in this paper by means of a non-linear optimization scheme involving the iterative Gauss-Newton (GN) method with Total Variation (TV) regularization, applied to two-dimensional (2D) body domains only. The proposed scheme is also compared to other traditional reconstruction algorithms like 2D back-projection and the sensitivity approximation to the Jacobian matrix of the system of equations governing EIT. Results from conductivity map reconstructions in anatomical phantoms have shown an improvement in signal-to-noise ratio (SNR) and distribution map error (DME) of 36% and 11% for the proposed non-linear method relative to the back-projection and single-step GN method with sensitivity approximation.

## 11 Introduction

12 Electrical Impedance Tomography as a medical imaging modality has been applied in the past years to the monitoring of several  
13 physiological events occurring inside tissues, with different degrees of success. Some examples include the measurement  
14 of pulmonary ventilation<sup>1,2</sup>, gastric emptying<sup>3,4</sup>, assessment of bone mineral density<sup>5</sup>, cardiac output<sup>6</sup>, brain function<sup>7,8</sup>,  
15 urodynamics<sup>9-11</sup>, as well as breast cancer screening<sup>12</sup>. Despite all these applications, EIT is yet to be regarded as a valid tool for  
16 routine clinical practice. Its lower spatial resolution when compared to other imaging modalities such as CT or MRI, combined  
17 with the complexity involved in the resolution of the so-called Inverse Problem for large scale domains (human body) further  
18 hinders the application of EIT in medicine<sup>3,13</sup>. However, the superior temporal resolution of EIT and the absence of ionization  
19 radiation during the imaging procedure, make this technique highly attractive as an extension to the bioimpedance method, by  
20 mapping the entire distribution of the internal conductivity of tissues into 2D medical images or 3D volumes from voltage  
21 measurements taken at the surface.

22 In conventional imaging modalities (e.g. X-rays in CT), a collimated beam of radiation passes through the body tissues  
23 in a straight line, and the attenuation of said beam is affected only by the material disposed along the path. So, CT can be  
24 defined as a local modality, meaning that internal *pixels* or *voxels* in the reconstruction maps affect only some of the boundary  
25 measurements. For the lower spectral range of EIT, scattering of the electric field over the body and nonlocal effects are more  
26 pronounced. Local change of conductivity typically induces variations on every voltage collected at the boundary, regardless of  
27 the current pattern injected inside the domain. As such, in order to find the distribution map for conductivity one must solve a  
28 system of simultaneous equations relating each domain element (*pixel* or *voxel*) to every measurement. It is also worth noting  
29 that EIT is not “tomographic” in the broader sense of the word, since it is not possible to reconstruct a map slice by slice due  
30 to the inability to confine electric currents to a single plane like X-rays, further increasing the complexity for conductivity  
31 estimation.

32 EIT has been traditionally classified as an ill-posed problem in accordance to Hadamard’s terminology<sup>14,15</sup>, due to the limited  
33 number of voltage measurements collected at the body surface for reconstruction, which combined with noisy measurements,

limited accuracy and numerical modelling errors lead to an inconsistent estimation of the conductivity distribution. Moreover, large variations in the internal conductivity map may be undetectable at the body surface for some measurement precision, compromising the uniqueness of the solution necessary for EIT. As such, ill-posed problems cannot be directly inverted without the introduction of *a priori* information or regularization to the model in order to attenuate the ill-posedness, as commonly done during the resolution of the Inverse Problem. In fact, several methods have been proposed in literature to tackle the non-linear behavior and ill-posed nature of EIT in the form of analytical approaches such as the back-projection algorithm<sup>16</sup>, global impedance<sup>17</sup> or variants to the traditional Gauss-Newton method, including single-step<sup>7</sup> and multi-step<sup>18</sup> reconstructions, the latter with iterative estimation of the conductivity map by re-calculating the Jacobian and Hessian matrices derived from the Taylor's series expansion of the EIT functional at every step. To cope with the computationally demanding calculation of the previous matrices, numerical approximations are often pursued by the sensitivity approach<sup>19</sup>, especially in large 3D domains, whereas the incorporation of a regularization term helps to stabilize the inverse process itself. Different penalty norms have been already suggested for EIT as alternatives to singular value decomposition<sup>17</sup> by Tikhonov<sup>7</sup>, Total Variation<sup>20,21</sup>, and Laplacian<sup>22</sup> regularizer, each of them penalizing conductivity estimates in terms of solution edges, amplitude, or slopes. Other methods are based on Bayesian approaches rather than on analytical or deterministic methods, since they allow to control and quantify some uncertainty parameters during the inversion process<sup>1</sup>, while accommodating different data models for EIT as *a priori* information. Still, results have shown that no significant improvement is reached by these methods relative to analytical ones<sup>23</sup>, potentially leading to unrealistic maps for conductivity distribution within medical images if too much weight is placed on the probabilistic model. Finally, some recent work with neural networks has been applied to EIT<sup>10</sup>, although more oriented for the post-processing of the conductivity estimate by comparing it to (offline) trained datasets and, thus, reducing the possible solution set for EIT.

However, the vast majority of the methods described above still use simple synthetic phantoms for reconstruction purposes, which are composed by a background conductivity map to which regular-shaped perturbation are added in a limited number, for the sake of solution convergence within acceptable processing times. In a medical point-of-view, this type of modelling is not accurate as tissues are highly irregular, with large conductivity contrasts and dispersed non-uniformly within the tomographic slice, thus influencing electric current propagation through the body and the distribution of the respective electric potential lines. In this paper, we propose a non-linear optimization scheme for the resolution of the Inverse Problem in EIT resorting to an iterative estimation for conductivity based on the Gauss-Newton method with TV regularization. The proposed method is applied to 2D conductivity distribution maps only (images), created from anatomical phantoms of internal body tissues contained inside tomographic slices, as 3D reconstructions are not yet suitable for the demanding computational method adopted in here. The estimates are then compared to other standard reconstruction methods involving theoretically less computational

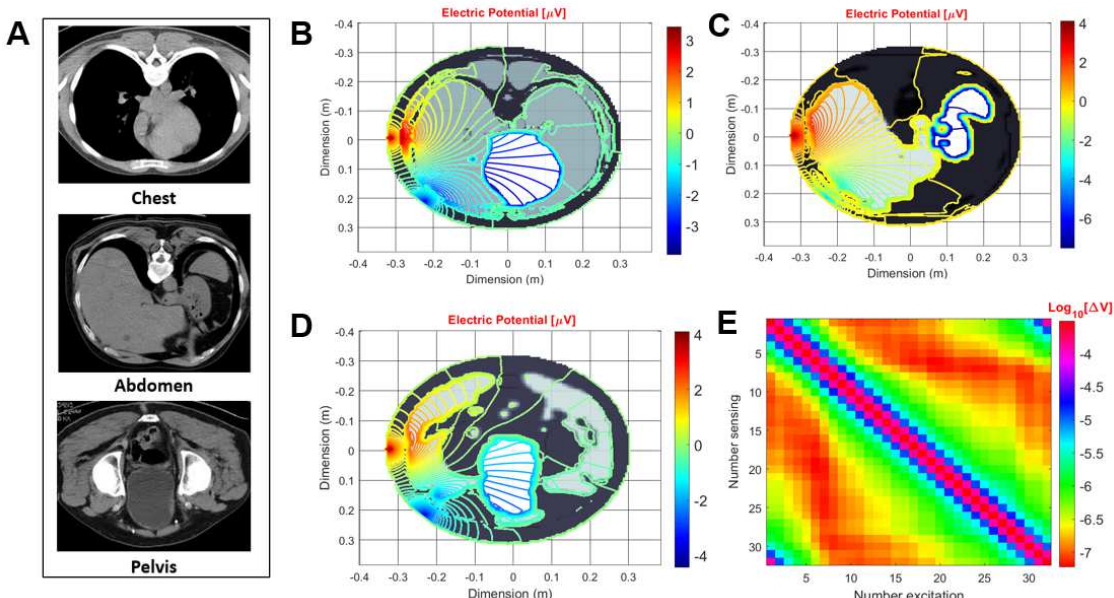


**Figure 1.** Resolution of the Forward Problem in EIT for medical images. **A.** MRI transverse slices from the chest, abdomen, and pelvic regions to be used as templates for the calculation of the electric potential distribution within these regions and imposed by off-body sources (electrodes). **B.** Potential distribution in the chest region when exciting from the left-side of the body. **C.** Potential distribution at the level of the liver (abdomen). **D.** Potential at the level of the urinary bladder (pelvic region). **E.** Potential difference (voltage) obtained at each electrode-sensing pair as a function of the excitation pair number (chest).

overload, including 2D back-projection and sensitivity approaches. Potential applications of this method include the estimation of many physiological parameters inside body tissues, circulating fluids and/or cavities, and suitable to be implemented *in situ* by wearable technology in the form of small standalone and energy-efficient platforms (e.g. epidermal electronics, lab-on-skin<sup>24</sup>), therefore avoiding massive numerical computations performed off-body (in servers or databases) for estimation of the distribution map for conductivity.

## Results

Transverse slices of anatomical structures present in the chest, abdomen and pelvic regions obtained by MRI were used to build the 2D computational domain for the EIT Forward Problem inside Matlab (MathWorks, Natick, MA, USA), as shown in Fig. 1A. The original medical images were down-scaled to dimensions of  $150 \times 150$  pixels with equal axis resolution (5 mm) in the  $x$ - and  $y$ -directions to facilitate spatial discretization and computational implementation. The relevant anatomical structures within each slice were identified in accordance with the image intensity levels present in the MRI scan, followed by the assignment of similar intensity *pixels* into clusters in order to identify (and label) different body tissues. Image filtering by means of a 10-by-10 Gaussian mask assisted in the removal of isolated *pixels* within the slices, while smoothing out transitions between clusters (tissues). Assignment of the conductivity value represented by  $\sigma$  to each tissue was done according to Table 1 in section **Forward Problem in EIT solved by FIT** from **Methods**, therefore yielding a  $\sigma$  map with a total of 22500 individual elements, whose barycenter is used to allocate the electric potential as dictated by FIT. By its turn, tissue stimulation for EIT uses a ring of electrodes equally distributed along the boundary of each anatomical slice, with current entering the body through a single electrode/element (source) and leaving by a different one (sink), as part of a current driving-pair of electrodes. Examples of the distribution of the electric potential ( $\phi$ ) in the anatomical phantoms for the chest, abdomen and pelvic regions are shown in Figs. 1B to 1E, obtained when stimulating by an electrode pair located on the left-side of the body and after the resolution of the Forward Problem in EIT. Different number of electrodes and current-injection protocols (that is, spacing

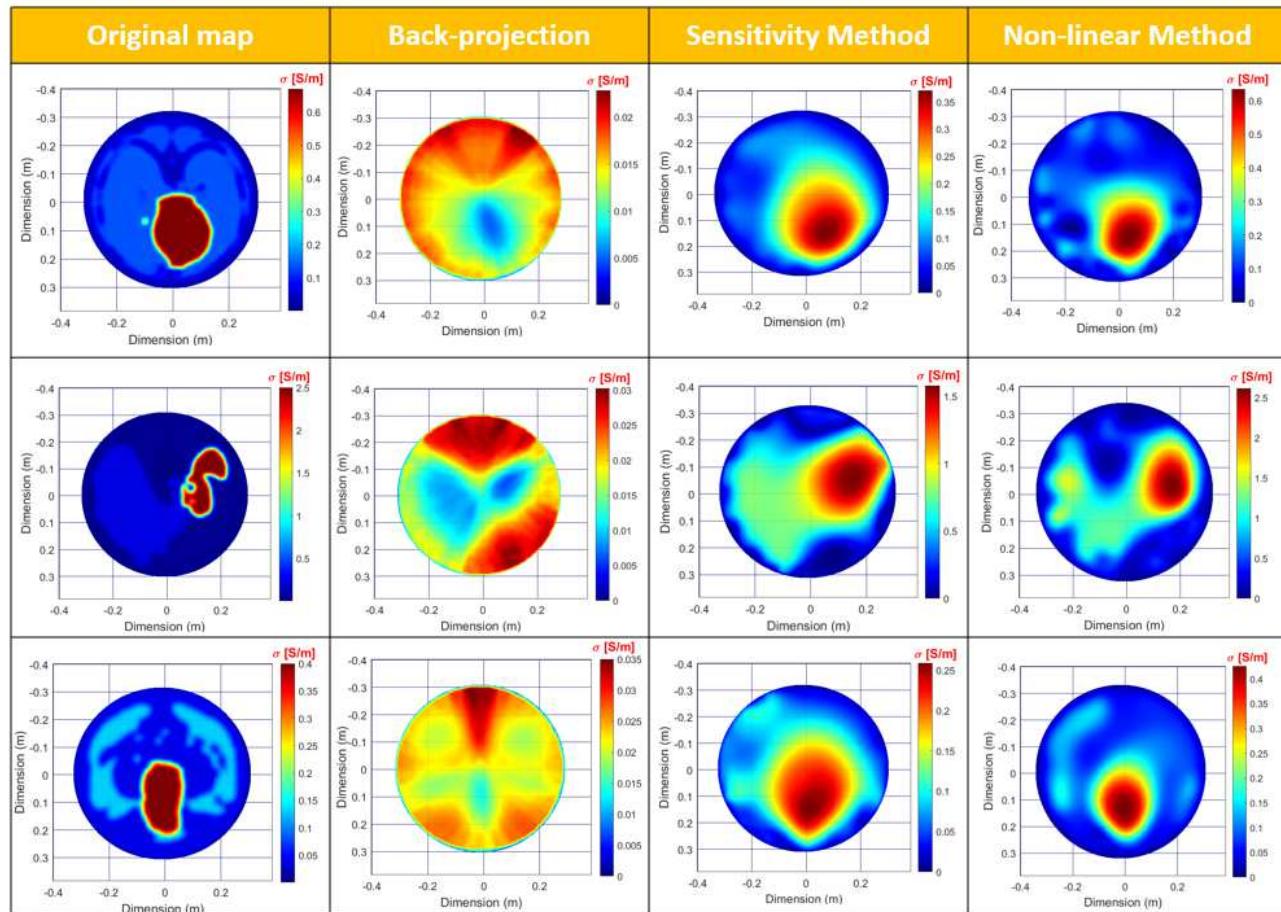


**Figure 2.** Conductivity reconstruction maps obtained by the three different methods (2D back-projection, GN with sensitivity and non-linear approaches) using 32 boundary electrodes, the adjacent electrode pair for current injection/measurement collection and SNR level of 30 dB for the collected vector of voltage potentials.

between source and sink electrodes) were also tested for performance comparison in the ensuing map estimations for  $\sigma$ .

Conductivity reconstruction maps for the several anatomical phantoms considered within the present manuscript are shown in Fig. 2, using the proposed non-linear methods and others (back-projection and sensitivity approaches) described in sections **Inverse Problem in EIT with non-linear optimization** and **Other reconstruction approaches** from **Methods**, respectively. In these reconstructions, the number of electrodes employed at the beginning of the reconstructions totalized 32, with the adjacent electrode pair protocol for current injection and measurements (voltage) collection. Additional white Gaussian noise was added to the measurements in order to mimic the effects of a real acquisition system in medical imaging. During the first reconstructions, the relation between measured power and added noise (or SNR) was set to a level of 30 dB, with the initial estimate for  $\sigma$  being a constant blank background.

For the back-projection method, a single iteration is used to obtain the reconstructed conductivity map from the relation between the projections and collected measurements with and without conductivity perturbations inside the domain during the resolution of the EIT Forward Problem, quite in a similar way as the single-step GN method with sensitivity approach. Regarding the proposed non-linear method, a total number of 10 iterations were used to improve reconstruction metrics, as long as the normalized error norm decreased monotonically along iterations. This error norm is given by Eq. 1, which employs the Euclidean length ( $l_2$ -norm) calculated between the estimated map at iteration  $p$  and the optimal  $\sigma^*$  distribution map.

$$\text{error norm} = \frac{\|\sigma^{(p)} - \sigma^*\|_2}{\|\sigma^*\|_2} \quad (1)$$

Since the number of degrees of freedom to be reconstructed within the maps is  $150 \times 150 = 22500$  and there are only  $(32 \times 32)/2 = 496$  independent measurements for a 32-electrode EIT system,  $\sigma$  reconstructions rely massively on the regularization term of the optimization functional. An evolution of the magnitude of the regularization parameter  $\lambda$  was performed within the range between  $1 \times 10^{-6}$  and  $1 \times 10^{-12}$  to assess its influence in the obtained error norm of the proposed non-linear GN method calculated for the last conductivity estimate (iteration). Figure 3A shows the result of this test for the three anatomical phantoms with a 32-electrode system and adjacent protocol. Since lower error norms were obtained for  $\lambda$  around  $1 \times 10^{-9}$ , this value was selected for the forthcoming reconstructions, whereas the parameters for  $\beta$  and  $\xi$  were set to  $1 \times 10^{-5}$  and  $1 \times 10^{-10}$ ,

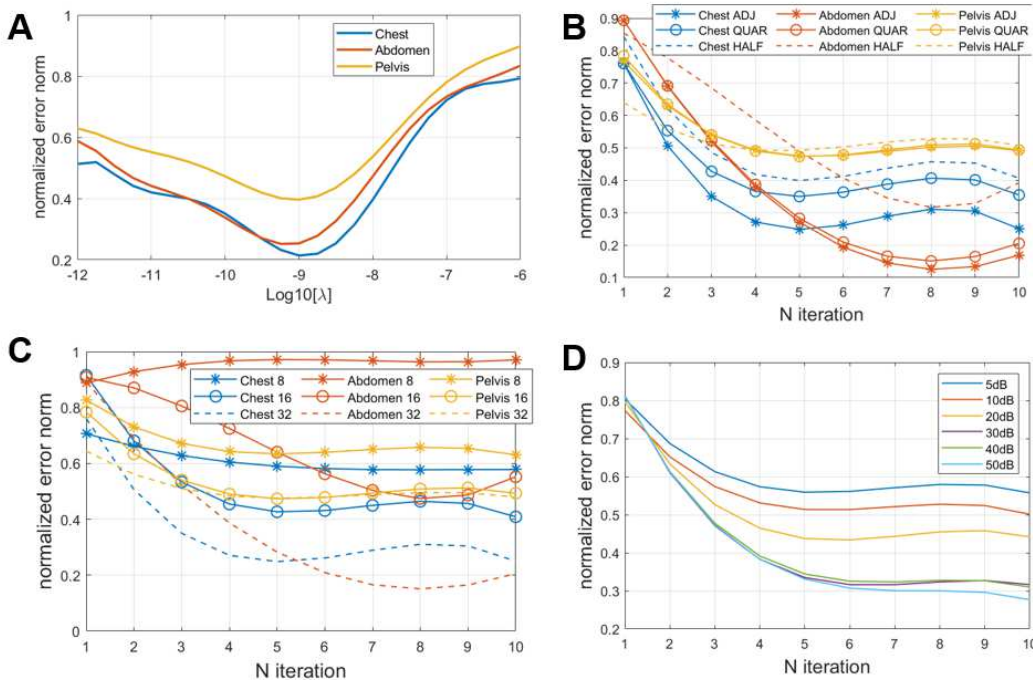


**Figure 3.** Performance metrics obtained for the chest, abdomen and pelvis phantoms, reconstructed by the proposed non-linear GN method. **A.** Evolution of the error norm as function of the regularization parameter  $\lambda$  used in the reconstruction routine for the three phantoms (32 electrodes, adjacent electrode pair protocol, SNR level of 30 dB). **B.** Evolution of the normalized error norm as a function of the number of iterations for the phantoms with the same number of boundary electrodes (32), SNR level (30 dB) and different injection protocols (adjacent, quarter or half). **C.** Error norm evolution with iteration number for the phantoms with the same injection protocol (adjacent electrode-pair), SNR level (30 dB) and different number of boundary electrodes (8, 16 or 32). **D.** Error norm evolution along iterations calculated as an average value between the phantoms subjected to different SNR levels (adjacent protocol with 32 boundary electrodes).

107 respectively, necessary to invert the system of equations for EIT (Eqs. 17 and 18) described in section **Inverse Problem in EIT**  
 108 with **non-linear optimization** from **Methods**.

109 Moreover, the influence of different initial conditions in the reconstruction methods was also studied to assess their  
 110 performance against varying factors such as the number of boundary electrodes (8, 16 or 32), type of protocol for current  
 111 injection/measurement collection (adjacent, quarter and half separation), as well as different magnitudes of added Gaussian  
 112 noise to the collected measurements (5, 10, 20, 30, 40 and 50 dB). The influence of different protocols on the error norm for a  
 113 32-electrode system subjected to SNR levels of 30 dB is shown in Fig. 3B. For this system, the adjacent protocol corresponds  
 114 to a contiguous electrode pair, quarter protocol to a separation of 8 electrodes (32/4) and half to 16 (32/2). By its turn, the  
 115 influence of different number of boundary electrodes is depicted in Fig. 3C, by resorting to the same adjacent protocol between  
 116 systems and SNR level (30 dB). Finally, the influence of different noise levels on the measurements obtained after the resolution  
 117 of the EIT Forward Problem is shown in Fig. 3D, again for a 32-electrode system with adjacent electrode pair protocol. From  
 118 the results, one can observe immediately that higher SNR levels (30 to 50 dB) produce almost similar error norms, hence the

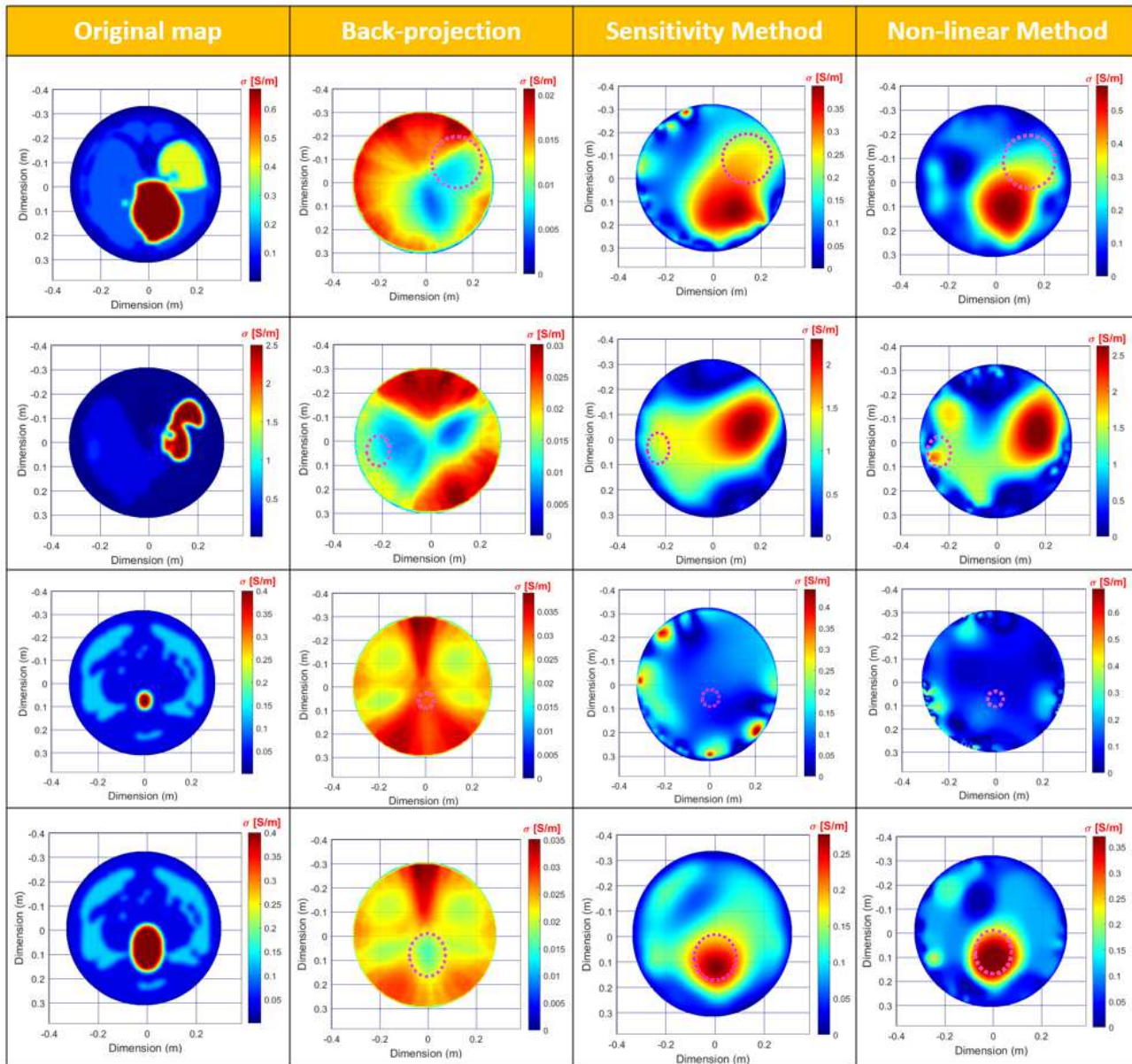


**Figure 4.** Conductivity reconstruction maps obtained for several tomographic slices located in the chest, abdomen and pelvis with affected areas (dashed circle) corresponding either to associated medical conditions (e.g., mass obstruction in the chest region and liver damage in the abdomen) or different volumes of enclosed conductivity (urine within the pelvis). These reconstructions were performed for the three numerical methods described within the manuscript (2D back-projection, GN with sensitivity and non-linear approaches) using a 32-electrode system with adjacent electrode pair protocol and SNR level of 30 dB.

use of a SNR level of 30 dB when depicting the previous reconstructed maps in Fig. 2. Similarly, 32-electrode systems with adjacent electrode pair protocol were selected due to the lower error norms achieved.

Additional reconstructions were performed using the same tomographic slices at different body levels, but now with associated conductivity disturbances, in an attempt to see if the different reconstruction methods could detect them. For the chest, a mass obstruction of the left main bronchus was created affecting the density of the surrounding soft tissue (lungs) and, consequently, its conductivity. For the abdominal phantom, a damage on the rightmost part of the liver led to tissue scarring (fibrosis), with irregular nodules replacing the smooth liver tissue as commonly found in the condition of cirrhosis. Within the pelvic region, 4 different volumes of urine contained inside the urinary bladder were tested in order to evaluate the performance of the reconstruction methods to monitor the physiological process of bladder filling with normal conductivity set for urine. The volumes tested were 50 ml (or residual volume), 150 ml, 300 ml, and 500 ml (full state). The results obtained for some of these reconstructions are shown in Fig. 4 for the 3 numerical methods, with both phantoms being imaged by a 32-electrode system running the adjacent electrode pair protocol and measurement noise level at 30 dB.

In order to achieve completeness in terms of image quality analysis for the reconstruction maps obtained amongst the different phantoms, numerical methods and (initial) imaging conditions, two standard metrics were employed, namely the signal-to-noise ratio for reconstructions (or  $\text{SNR}_{\text{recon}}$ ) and distribution map error (DME<sub>recon</sub>) given by Eqs. 2 and 3, respectively, with  $\sigma_{i,j}^*$  representing the conductivity at pixel  $(i,j)$  in the optimal map, and  $\sigma_{i,j}$  for the reconstructed map.

$$\text{SNR}_{\text{recon}}(\sigma^{(p)}) = 20 \log \left[ \frac{\max(\sigma^{(p)} - \sigma^*) - \min(\sigma^{(p)} - \sigma^*)}{\text{std}(\sigma^{(p)} - \sigma^*)} \right] \quad (2)$$

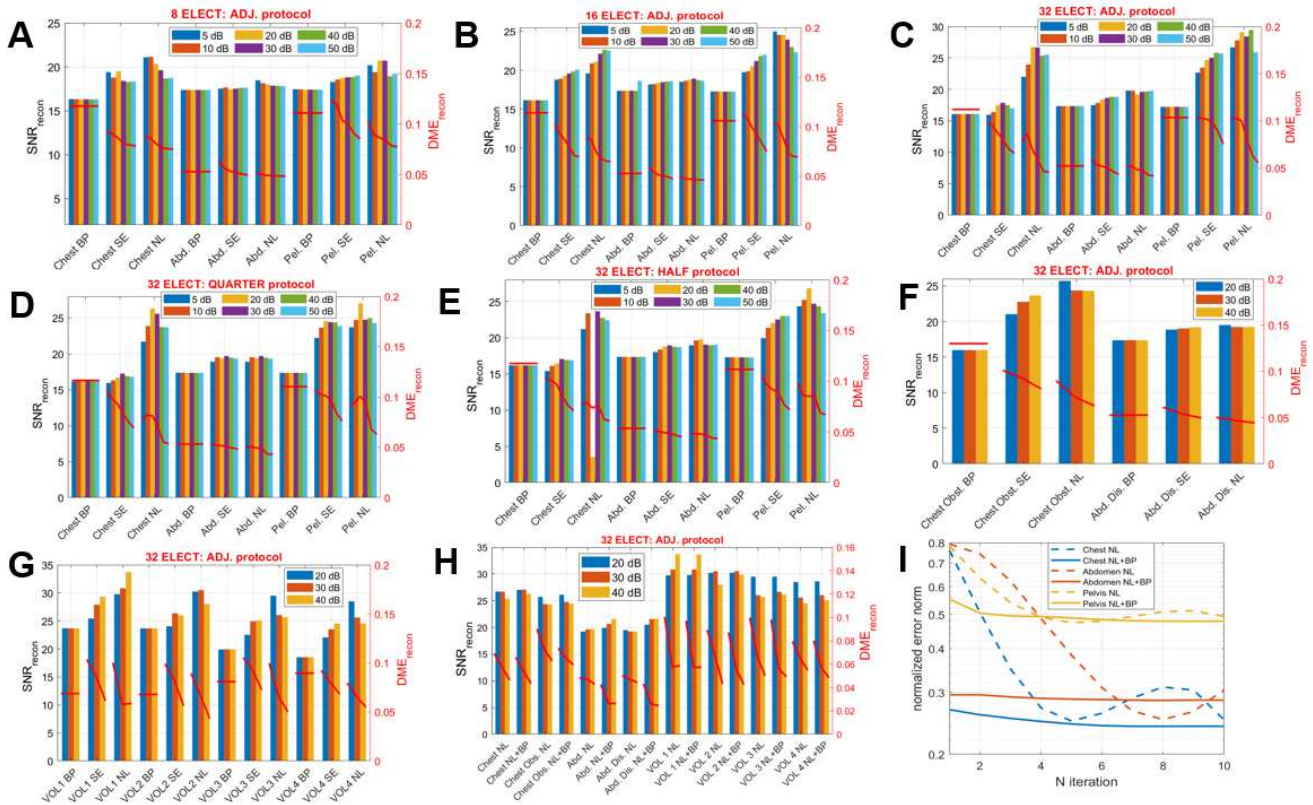


**Figure 5.** Performance metrics employed for quality assessment of the reconstruction maps for  $\sigma$  obtained by the numerical methods, under the influence of different initial conditions. **A.** Evolution of  $\text{SNR}_{\text{recon}}$  (left) and  $\text{DME}_{\text{recon}}$  (right) metrics for the chest, abdominal and pelvic phantoms using the 2D back-projection (BP), GN with sensitivity (SE) and non-linear (NL) approaches, in the condition of 8 boundary electrodes, adjacent electrode pair protocol and several SNR levels affecting the collected measurements. **B.** Same metrics evolution obtained when employing 16 boundary electrodes. **C.** Metrics evolution for a 32-electrode system using the quarter injection/measurement protocol (separation of 8 electrodes). **D.**  $\text{SNR}_{\text{recon}}$  and  $\text{DME}_{\text{recon}}$  metrics for a 32-electrode system using the half injection/measurement protocol (separation of 16 electrodes in the 32-electrode system). **F.** Evolution of the performance metrics for the anatomical slices with associated medical conditions in the chest and abdominal phantoms (32-electrode system, adjacent electrode pair protocol and three SNR levels of added noise: 20, 30 and 40 dB). **G.** Same metrics for the condition of varying urinary bladder volume (4 discrete levels labelled from 1 to 4). **H.** Evolution of the performance metrics for all the tested phantoms, with initial blank conductivity distribution (NL) or estimate from the 2D back-projection method (NL+BP), used as the first iteration of the non-linear GN method. **I.** Evolution of the image error norm along the iterations of the proposed non-linear GN method for the chest, abdominal and pelvic phantoms (32-electrode system, adjacent electrode pair protocol, 20 dB SNR) with different initial conductivity map estimate: blank distribution (NL) and derived from back-projection (NL+BP).

$$DME_{recon}(\sigma^{(p)}) = \frac{1}{N^2} \sum_{i,j}^N \frac{|\sigma_{i,j}^{(p)} - \sigma_{i,j}^*|}{\max(\sigma^*) - \min(\sigma^*)} \quad (3)$$

For the 2D back-projection and GN method with sensitivity approach, only the first iteration ( $p = 0$ ) was evaluated by the previous metrics, whereas for the proposed GN method with non-linear optimization approach the last iteration ( $p = 10$ ) was evaluated. The evolution of the metrics is plotted on a bar graphic for  $\text{SNR}_{recon}$  on the left axis of Figs. 5A to 5C, while  $DME_{recon}$  appears as a superimposed red curve along the bars, whose magnitude is shown on the right axis. These first plots exhibit the influence of different electrode systems (8, 16 and 32) on the metrics for the adjacent protocol, while testing the five noise levels allowed to the collected measurements (5, 10, 20, 30, 40 and 50 dB). Subsequent plots show the influence of the quarter and half current injection/measurement collection on the  $\text{SNR}_{recon}$  and  $DME_{recon}$  metrics for a 32-electrode system only, and for the different phantoms and reconstruction methods within Figs. 5D and 5E, respectively. For the tomographic slices representing medical conditions and bladder volume monitoring, the metrics were only evaluated with noise levels of 20, 30 and 40 dB inside 32-electrode systems (adjacent protocol), as they exhibited better performance results (Figs. 5F and 5G).

Finally, one last experiment was carried out to assess the influence of the initial conductivity estimate in the proposed non-linear method. The constant conductivity background (NL) was tested against the reconstruction estimate provided by the 2D back-projection method (NL+BP) and used as the initial conductivity map entering the GN method (iteration zero). The performance metrics achieved by this experiment are gathered together in Fig. 5H, for all the tested phantoms (with and without perturbations) inside a 32-electrode system with adjacent protocol for current injection/measurement collection. Furthermore, the evolution of the average error norm along the iterations for each slice (chest, abdomen and pelvis) was also recorded in Fig. 5I, for the non-linear GN method with initial blank distribution (NL) for  $\sigma$ , as well as retrieved from the back-projection method in the first iteration (NL+BP). At the end, Fig. 6 shows the reconstructed conductivity maps obtained by the (NL+BP) method inside the chest phantom (Figs. 6A and 6B), abdomen (Figs. 6C and 6D) and pelvis (Figs. 6E to 6H), the latter ones with several volumes of stored urine within the bladder walls.

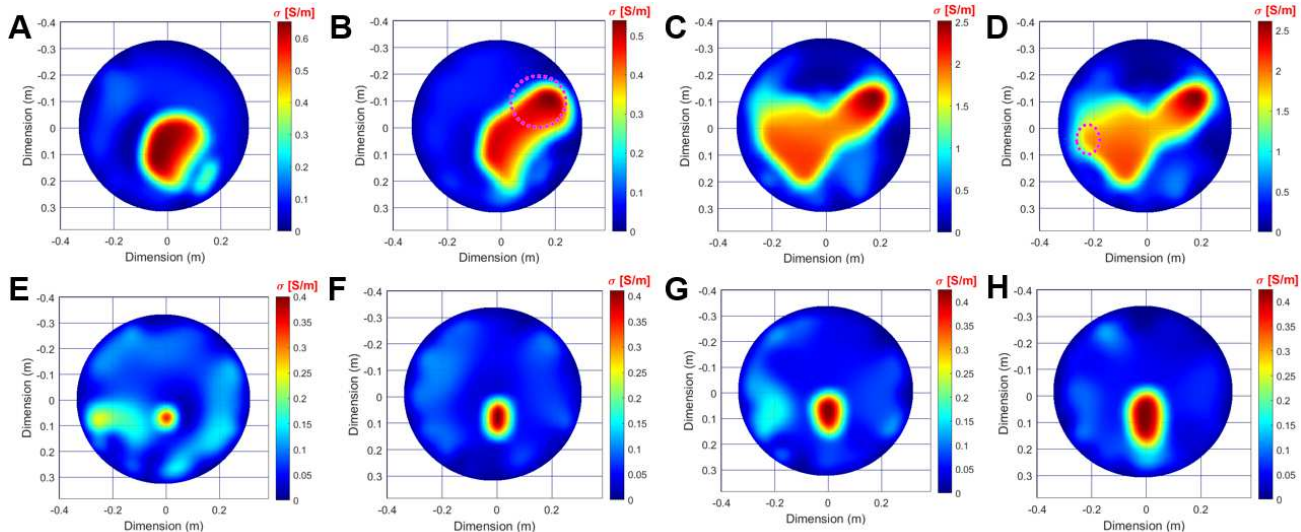


**Figure 6.** Conductivity reconstruction maps obtained for the proposed non-linear method with TV regularization and initial estimate obtained by the 2D back-projection method (32-electrode system, adjacent electrode pair protocol, SNR level of 20 dB). **A.** Chest phantom. **B.** Chest phantom with mass obstruction of the lung tissue encircled by the pink dashed circle. **C.** Abdominal phantom. **D.** Abdominal phantom with affected tissue damage inside the liver. **E.** Pelvic phantom with residual urinary bladder volume. **F.** Pelvic phantom with a lower intermediary volume contained inside the bladder walls. **G.** Pelvic phantom for a higher intermediary bladder volume. **H.** Pelvic phantom closer to the condition of full urinary bladder volume.

## 155 Discussion

The results obtained within this manuscript have shown better performance metrics for the conductivity reconstruction maps when using larger number of boundary electrodes (32), which yields more independent measurements as seen both for the evolution of the error norm along iterations (Fig. 3C) and  $\text{SNR}_{recon}/DME_{recon}$  metrics (Figs. 5A to 5C), regardless of the added noise levels or tested phantoms. Only the previous metrics for the 2D back-projection method remain fairly constant between different electrode systems. For the two GN methods tested (sensitivity and non-linear approaches), the  $\text{SNR}_{recon}$

161 levels increase for SNR above 20 dB, with  $DMR_{recon}$  following a steep decreasing trend. Regarding the influence of the current  
162 injection/voltage measurement protocol (within Figs. 3B, 5C to 5E), better performance metrics were achieved for the adjacent  
163 protocol, followed by the quarter and half ones. This situation is also reported on other literature sources<sup>1,22</sup> where the adjacent  
164 electrode pair protocol seems to be the most standard system in-use for EIT. Reasons for this selection may be attributed to  
165 local current spreading effects occurring closer to the driving-pair, which influence more decisively the nearby voltage-sensing  
166 electrodes relative to the half and quarter protocols, wherein effects of electric current propagation are recorded more distantly  
167 and, therefore, dissipated evenly throughout the entire simulation domain.

168 In terms of qualitative assessment of the  $\sigma$  reconstructions obtained by the three numerical methods, the 2D back-projection  
169 clearly identifies with great detail the natural contours of internal body tissues or organs; however, the obtained  $\sigma$  levels are still  
170 1 to 2 orders of magnitude lower than the original or optimal distribution map (Fig. 2). By its turn, tissue contours obtained  
171 by the single-step GN method with sensitivity approximation and proposed non-linear approach appear more blurred in the  
172 images, though the true conductivity levels are eventually recovered by the latter method, especially in the maps with higher  
173 conductivity contrasts between internal tissues and background. This also helped to identify with more precision the affected  
174 areas associated with medical conditions inside the chest and abdominal regions, while tracking better the volume of stored  
175 urine within the pelvic region, except for the residual volume state (Fig. 6). In addition, better  $SNR_{recon}$  and  $DME_{recon}$  metrics  
176 were achieved with the proposed non-linear method as seen in Figs. 5F and 5G. In general, there is an improvement of 36%  
177 and 11% of the performance metrics for the proposed method relative to the back-projection and single-step GN method with  
178 sensitivity approach, respectively. Moreover, the influence of added noise levels within the collected measurements is more  
179 pronounced when tracking the bladder volume, wherein the 20 dB level surpasses that obtained with the 30 and 40 dB levels for  
180 larger bladder volumes (3 and 4) in the  $SNR_{recon}$  metric. However, the  $DME_{recon}$  decisively follows an opposite trend.

181 Regarding the choice of the initial conductivity estimate for the proposed non-liner method, the use of  $\sigma$  estimates  
182 obtained directly from the back-projection method has proved to yield slightly better results than blank  $\sigma$  distributions, with  
183 an improvement of roughly 6% between recorded performance metrics (Fig. 5H). Perhaps, the most evident advancement  
184 yielded by the use of an initial back-projection estimate is the steep decrease of the error norm during the first 4 iterations of the  
185 non-linear GN method (Fig. 5I), followed by its convergence to the final error norm. In the last reconstructions in Fig. 6, both  
186 the contours and magnitude of the internal tissues composing each slice are best approximated by the (NL+BP) method relative  
187 to the non-linear GN method alone (NL). Indeed, back-projection seems to contribute to the correct identification of internal  
188 tissue borders and limits within the slices due to the current spreading effect employed by this algorithm, leaving initial “seeds”  
189 of tissue conductivity values to be recovered later by the GN method at a faster convergence rate.

190 Finally, the proposed non-linear method does not come with some limitations. To start with, the method itself was only  
191 applied to 2D domains (images) with equivalent dimensions for the different tomographic slices tested, which in reality might  
192 not reflect the true anatomy of some body segments. Secondly, confinement of EIT currents to a single anatomical slice is hardly  
193 verified in practice since current streamlines propagate in all the three directions according to the local conductivity distribution  
194 between source and sink points. On the other hand, 3D reconstructions were impractical to achieve by the current method  
195 due to the overall dimensions of the (non-linear) system of equations to be inverted. For this scenario, other reconstruction  
196 methods must be pursued, including the 3D back-projection method, and also taking advantage of parallel computation instead  
197 of sequential inversion. The fact that only the single-step GN method with sensitivity approach was used for performance  
198 comparison with the proposed method (and not its multi-step counterpart) had to do with the amount of processing time  
199 required to solve a single iteration, sometimes even longer than that for the entire non-linear approach ( $\approx 5$  minutes). Possibly,  
200 the discrepancy in terms of the dimensions of the system of equations yielded by the sensitivity approach and the sparsity  
201 level involved contributed both to this phenomenon. Other numerical methods involving post-processing of the collected  
202 measurements or the final reconstructed maps are also associated with novel digital processing techniques (e.g., supervised  
203 learning classification<sup>10</sup> and Bayesian learning<sup>23</sup>) that help circumvent the ill-posed nature of the EIT Inverse Problem but  
204 without completely solving it.

## 205 Methods

### 206 Forward Problem in EIT solved by FIT

207 The set of equations governing the Forward Problem in EIT have long been derived, by making use of some mathematical  
208 simplifications applied to the Ampere’s Law in the harmonic regime of wave propagation, stating that all the magnetic  
209 phenomena inside the simulation domain is negligible and the electric field irrotational ( $\nabla \times \mathbf{E} = 0$ ), thus originated from  
210 the gradient of a scalar potential,  $\phi$ . These conditions force the continuity equation in Physics<sup>25</sup> by preserving the electric  
211 fluxes over the computational domain  $\Omega$  except in the elements where the electric current flows in and out (driving or injection

212 electrode pair), as given by Eq. 4.

$$\begin{cases} \sigma \mathbf{grad}\phi^{in} = -\sigma \mathbf{grad}\phi^{out}, & \text{driving-pairs} \\ \mathbf{div}(\sigma \mathbf{grad}\phi) = 0, & \text{elsewhere} \end{cases} \quad (4)$$

213 The knowledge in advance of the complete distribution map for conductivity ( $\sigma$ ), as well as the topological operators for  
214 gradient (**grad**) and divergence (**div**) enables the computation of the scalar potential as the solution of the Forward Problem in  
215 EIT all over the domain, specially at the boundary where voltage-sensing electrodes (when different from the current-driving  
216 ones) collect the difference in potential between locations encompassed by an electrode pair, or relative to a common potential  
217 reference<sup>3</sup>. In practice only a finite number of electrodes is employed, with the voltage-sensing and current-driving electrodes  
218 sharing the same location (equivalent pair, but different functionality), which yields a finite number  $N_v$  of possible voltage  
219 measurements. These can form a data vector of the form  $V = [v_1, v_2, \dots, v_{N_v}]$  that is related to the  $\sigma$  map by mapping matrix  $F_\sigma$ ,  
220 as stated in Eq. 5.

$$F_\sigma(\sigma) = V \quad (5)$$

221 This is the formulation of the Forward Problem in EIT, and the Inverse Problem requires the recovery of  $\sigma$  by knowing  $V$ .  
222 In this study, the Forward Problem for 2D domains (images) will differ slightly from that within Eq. 5. The approach is to  
223 confine all the information on  $\sigma$  to an operator  $A$  and apply it to the set of potentials  $\phi = [\phi_1, \phi_2, \dots, \phi_{N_v}]$ , as done in Eq. 6.

$$A(\sigma)\phi = V \quad (6)$$

224 Discretization of Eq. 4 for 2D domains is achieved in the current study by resorting to the framework employed by the  
225 Finite Integration Technique (FIT)<sup>26,27</sup>. This yields the following discretized system of equations,

$$\mathbf{div}(\Lambda \mathbf{grad}\phi) = 0, \quad \text{except driving-pairs} \quad (7)$$

226 where  $\mathbf{grad} = [D_h \ D_v]^T$  is a matrix composed by 1<sup>st</sup> order horizontal ( $D_h$ ) and vertical ( $D_v$ ) differences for each pixel (element)  
227 in the image;  $\mathbf{div} = [D_h \ D_v]$ ; and matrix  $\Lambda = \begin{bmatrix} P_h \sigma & 0 \\ 0 & P_v \sigma \end{bmatrix}$  contains an average of  $\sigma$  in each space direction.

228 The EIT system of equations just described was applied to 2D anatomical slices of the chest, abdomen and pelvic regions,  
229 whose main structures were assigned the conductivity levels present in Table 1. The numerical system was implemented  
230 in the form  $\mathbf{Au}=\mathbf{b}$ , with matrix  $\mathbf{A} \in \Re^{N_e \times N_e}$  ( $N_e$  = number of domain elements) containing the product of the topological  
231 operators with conductivity,  $\mathbf{b} \in \Re^{N_e \times N_v}$  an all-zero column matrix except in the elements driving current and  $\mathbf{u} \in \Re^{N_e \times N_v}$   
232 the solution in terms of  $\phi$ . Inversion of the system ( $\mathbf{u}=\mathbf{A}^{-1}\mathbf{b}$ ) was achieved within a couple of seconds of processing time  
233 without pre-conditioning the highly sparse matrix  $\mathbf{A}$ , using an Intel Core i7-4770 (3.4 GHz) processor and 16 MB of RAM.  
234 Examples of the distribution of the electric potential for the considered anatomical slices are presented in the **Results** section of  
235 this manuscript.

236 Finally, in order to complete the forward model in a real case scenario, it is necessary to build a measurement matrix  $M$   
237 containing all the voltages captured at the sensing positions for every current pattern driven by an electrode pair. For simplicity,  
238 the number of voltages and current patterns are equal ( $N_v$ ), which gives a total of  $(N_v \cdot N_v)$  measurements per acquisition frame  
239 inside the proposed EIT system. Applying matrix  $M$  to the potentials allows to write the form,

$$d = M\phi + \eta \quad (8)$$

240 where  $d \in \Re^{(N_v \cdot N_v) \times N_v}$  is the real potential generated in each sensing electrode by every current pattern ( $M \in \Re^{(N_v \cdot N_v) \times N_e}$ ,  $\phi \in \Re^{N_e \times N_v}$ ) and  $\eta$  is an error term that mimics the effect of noise acquired during the measurement process.

## 242 Inverse Problem in EIT with non-linear optimization

243 The Inverse Problem in EIT can be seen as the process to find the optimal conductivity distribution map minimizing Eq. 9.

$$\sigma^* = \arg \min \sum_{i=1}^{N_v} \| F_i(\sigma) - d_i \|_2^2 + \lambda \| R(\sigma) \|_{l_p} \quad (9)$$

244 The first term on the right-hand side is the data term that tries to fit the measured data to the forward model in a least  
 245 square sense, whereas the second term is a regularization (or image) term that uses *a priori* information to compensate for the  
 246 information loss due to the EIT process (measurement error, noise, etc.), thereby reducing the solution set for  $\sigma$ :  $R(\sigma)$  is a given  
 247 penalty function and  $\lambda$  the regularization parameter. The choice of the  $l_p$ -norm involved in the image term also contributes for  
 248 the type of conductivity estimation obtained by Eq. 9. For example, the Tikhonov regularization is a least square norm ( $l_2$ -norm)  
 249 that penalizes transitions within the  $\sigma$  map, smoothing out solution edges<sup>14</sup>. By its turn, Total Variation (TV) is an  $l_1$ -norm of  
 250 the spatial image gradient that penalizes transitions on the amplitude and not its slope. Therefore, the  $l_1$ -norm penalty is smaller  
 251 for a data outlier than  $l_2$ -norm, a candidate for superior performance in the recovery of conductivity discontinuities commonly  
 252 found within biological tissues. Nevertheless, the solution obtained by  $l_1$ -norm involves the minimization of a non-differential  
 253 function of the form,

$$\| R(\sigma) \|_1 = \Psi_{TV}(\sigma) = \int_{\Omega} |\nabla \sigma| dr = \int_{\Omega} \left[ \sqrt{\sum_{k=1}^K \left( \frac{\delta \sigma}{\delta r_k} \right)^2 + \beta^2} \right] dr \quad (10)$$

254 where  $K$  is the number of dimensions within domain  $\Omega$  and  $\beta$  is a constant that ensures TV is differentiable when gradients are  
 255 close to zero. The discrete version of TV for a  $K$ -dimensional space is given below as<sup>30</sup>,

$$\Psi_{TV}(\sigma) = \sum_{n=1}^{N_e} \left( \sqrt{\sum_{k=1}^K (D_k^n \sigma)^2 + \beta^2} \right) (\Delta r)^K \quad (11)$$

256 evaluated in all the elements of the domain ( $N_e$ ) and gradient ( $D$ ) for each space direction. Using TV as the regularizer and the  
 257 adopted settings in the current manuscript for the Forward Problem, the Inverse Problem can be fully described by Eq. 12: for a  
 258 fixed  $\lambda$ , this corresponds to a non-liner optimization problem for  $\sigma$ <sup>31</sup>.

$$\begin{aligned} \sigma^* &= \arg \min \sum_{i=1}^{N_v} \| M\phi_i - d_i \|_2^2 + \lambda \Psi_{TV} \\ \text{s.t. } A(\sigma)\phi_i &= v_i, \quad d_i = M\phi_i + \eta \end{aligned} \quad (12)$$

259 The mathematical derivations present so far have been arranged in order to solve the Inverse Problem iteratively by the  
 260 Gauss-Newton (GN) method, which combines  $2^{nd}$ -order information obtained by the expansion in Taylor's series of the  
 261 objective function in optimization, with approximations to the Hessian matrix ( $2^{nd}$  derivatives) made by the product of the  
 262 Jacobian ( $1^{st}$  derivatives) and its transpose, as minimization to the sum of squared objective functions<sup>31,32</sup>. The gradient of  
 263 Eq. 12 is thus fundamental to define the iterative scheme as,

$$G_{EIT} = \sum_{i=1}^{N_v} [G_{LS}]_i + \lambda G_{TV} \quad (13)$$

264 where  $[G_{LS}]_i$  is the gradient of the  $i^{th}$  least square data term and  $G_{TV}$  the gradient of the TV regularizer. The gradient for the  
 265 data term is calculated by making use of the properties of the derivative for  $l_2$ -norms as Eq. 14 attests.

$$[G_{LS}]_i = \frac{\partial (\| MA^{-1}(\sigma)v_i - d_i \|_2^2)}{\partial \sigma} = \frac{\partial [MA^{-1}(\sigma)v_i]^T}{\partial \sigma} [MA^{-1}(\sigma)v_i - d_i] = J_{r_i}^T \cdot r_i \quad (14)$$

Table 1. Conductivity of some body tissues present in the anatomical phantoms used in the current manuscript<sup>22,28,29</sup>.

Tissue	$\sigma$ (S/m)	Tissue	$\sigma$ (S/m)
Heart	0.67	Stomach (pH 2.5)	2.5
Lung	0.138	Urinary Bladder	0.4
Liver	0.14	Bone	0.006
Subcutaneous tissue	0.04	Air <sup>1</sup>	$1 \times 10^{-1}$
Muscle	0.13		

Note: <sup>1</sup>The conductivity of air (free space) is zero, however, for the purpose of numerical stability, it was assigned a small non-zero value.

266 The quantity  $J_{r_i}$  is the Jacobian of each Forward Problem involving an active current source and  $r_i$  the  $i^{th}$  residual term.  
267 Further developments on the Jacobian term, namely by means of the properties for the inverse matrix, allow to obtain Eq. 15.

$$J_{r_i} = \frac{\partial [MA^{-1}(\sigma)v_i]}{\partial \sigma} = -MA^{-1}\frac{\partial [A(\sigma)\phi_i]}{\partial \sigma} = -MA^{-1}C_{r_i} \quad (15)$$

268 Finally, the expression for the gradient of the  $i^{th}$  least square data term for the EIT Inverse Problem is given by Eq. 16.

$$[G_{LS}]_i = -C_{r_i}^T [A^{-T}(M^T \cdot r_i)] \quad (16)$$

269 For the TV functional, the gradient is obtained by the 1<sup>st</sup>-order derivative applied to the discrete version of TV in Eq. 11,  
270 yielding the expression below.

$$G_{TV} = (\Delta r)^K \sum_{n=1}^{N_e} \sum_{k=1}^K \frac{[D_k^n](D_k^n \sigma)}{\sqrt{(D_k^n \sigma)^2 + \beta^2}} \quad (17)$$

271 The optimization problem in EIT just described converges to its global minimum if the system is convex. So, a quadratic  
272 bound for the system of equations in Eq. 12, is desirable. Within the adopted formulation, one should note that the data term is  
273 already quadratic, whereas, for the image term, the authors of study<sup>33</sup> have demonstrated that the TV regularizer adopted in the  
274 current manuscript can be used as a quadratic majorizer by applying some algebraic manipulation to the 1<sup>st</sup>-order expansion in  
275 Taylor's series for the square root function. With the latter quadratic bound fulfilled, the iterative update of the Gauss-Newton  
276 algorithm applied to the Inverse Problem can be given as,

$$\begin{cases} \sigma^{(p+1)} = \sigma^{(p)} + \Delta\sigma \\ \Delta\sigma = - \left[ \sum_{i=1}^{N_v} [J_{r_i}^T \cdot J_{r_i}]^{(p)} + \lambda \frac{G_{TV}(\sigma^{(p)})}{\sigma^{(p)}} + \xi Id \right]^{-1} \cdot \left[ \sum_{i=1}^{N_v} [J_{r_i}^T \cdot r_i]^{(p)} + \lambda G_{TV}(\sigma^{(p)}) \right] \end{cases} \quad (18)$$

277 where  $\Delta\sigma$  is the conductivity update,  $p$  the current iteration,  $p+1$  the next iteration,  $\xi$  the Levenberg-Marquardt parameter and  
278  $Id$  the identity matrix. Reconstruction of distribution maps for conductivity inside 2D domains were presented in the **Results**  
279 section only. To that end, the 2D discrete version of  $G_{TV}$  was re-written in a more compact way as,

$$G_{TV}(\sigma) = (\Delta r)^2 (D^T W D) \sigma \quad (19)$$

280 with  $\Delta r$  being the domain resolution for both axis directions (square image), while  $D$  is defined as  $D = [(D_h)^T \quad (D_v)^T]^T$ , and  $W$   
281  $= \begin{bmatrix} \text{diag}(w(\sigma)) & 0 \\ 0 & \text{diag}(w(\sigma)) \end{bmatrix}$ , with diagonal entries given by  $w(\sigma) = \left[ \frac{1}{\sqrt{(D_h^n \sigma)^2 + (D_v^n \sigma)^2 + \beta^2}}, n = 1, \dots, N_e \right]$ .

## 282 Other reconstruction approaches

283 Linear reconstruction methods for EIT assume that a small perturbation in conductivity inside the domain will produce a  
284 linear change on the voltage measurements at the boundary. One of the most common linear approximations is the so-called  
285 2D back-projection algorithm for EIT based on the work by Santosa and Vogelius<sup>16</sup>. The algorithm consists in assigning to  
286 every *pixel* within the image the corresponding electric potential registered at the boundary by following the electric field lines  
287 originating from *pixel* location until they reach the first *pixel* (or element) in the surrounding boundary. Besides depending on  
288 *pixel* location, these equipotential lines are largely influenced by the pattern in which the current is injected through a pair of  
289 electrodes or, equivalently, the electric dipole at the boundary, as shown in Figs. 7A to 7C.

290 Since the continuous domain boundary cannot be covered in its entire extension by a discrete number of electrodes, the  
291 site at which the equipotential line terminates usually does not correspond to a surface electrode but, instead, to an elsewhere  
292 location in-between two adjacent electrodes. In these cases, the potential registered at the surface electrode that is closer to the  
293 line termination is assigned to the inner *pixel*. This way, a mapping operator denoted by  $P_m$  is created for every rotation of the  
294 dipole position and within the same current-injection protocol. When both data vectors containing the voltage measurements  
295 for the disturbed and undisturbed (original) conductivity map are available, the disturbed image map ( $\delta\sigma$ ) can be obtained as,

$$\delta\sigma_j + \sigma_j = -\frac{1}{M} \sum_{m=1}^M \frac{P_m(\delta\sigma_j + \sigma_j)}{P_m(\sigma_j)} \cdot \sigma_j \quad (20)$$

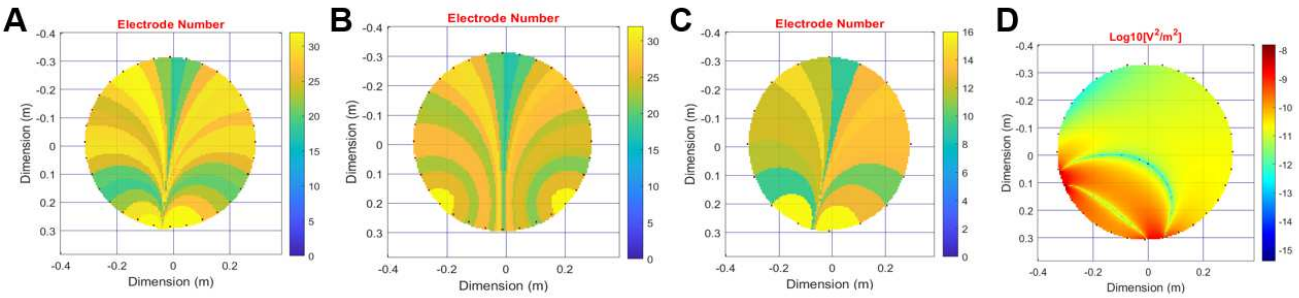


**Figure 7.** Intermediary maps obtained during the resolution of the Inverse Problem in EIT. **A.** Back-projection operator obtained using adjacent pair injection of current on a 32-electrode arrangement, with source and sink located in the bottom-most part of the phantom. **B.** Back-projection operator obtained for an 8-electrode spacing between source and sink on the same arrangement. **C.** Back-projection operator with adjacent pair injection of current on a 16-electrode arrangement. **D.** Sensitivity distribution for electrode pairs with different current injection and voltage detection numbers (32-electrode arrangement).

where  $j$  represents the image pixel and  $m$  is the number of dipole rotations.

Finally, conductivity map estimation using the sensitivity approach is based on the substitution of the Jacobian matrix in Eq. 18 by an approximation derived from the Gaselowitz's theorem<sup>34</sup>. This theorem gives a rational to evaluate the measurements' effectiveness in sampling  $\sigma$  variations inside a domain in the static or quasi-static electromagnetic scenarios<sup>35,36</sup>. It is derived initially from the Lorentz's reciprocity theorem for the case of two arbitrary systems – denoted by 1 and 2 – of electric fields produced by a pair of sources inside a finite spatial domain, also referred to as the direct and adjoint fields respectively. For EIT, the electric field is obtained from the gradient of a scalar potential and the difference in potential between two systems is the voltage. In multi-systems with a large number of current sources, variation in measurements due to a change in  $\sigma$  is expressed as,

$$\Delta\phi = S\Delta\sigma \quad (21)$$

where  $S$  is the sensitivity matrix, whose entries are calculating according to Eq. 22 for a limited number  $N_v$  of equivalent current sources with the same magnitude ( $I$ ). An example of a distribution pattern of  $S$  for a different electrode pair number used for current injection and voltage detection is shown in Fig. 7D.

$$S_{i,j,i \neq j} = \frac{1}{I^2} (\nabla\phi_i \cdot \nabla\phi_j) \quad (22)$$

Replacement of the Jacobian matrix by the sensitivity equivalent gives the iterative update of the GN method in the form of Eq. 23.

$$\begin{cases} \sigma^{(p+1)} = \sigma^{(p)} + \Delta\sigma \\ \Delta\sigma = - \left[ \sum_{i=1}^{N_v} [S^T \cdot S]^{(p)} + \lambda \frac{G_{TV}(\sigma^{(p)})}{\sigma^{(p)}} + \xi Id \right]^{-1} \cdot \left[ \sum_{i=1}^{N_v} [S^T \cdot r_i]^{(p)} + \lambda G_{TV}(\sigma^{(p)}) \right] \end{cases} \quad (23)$$

For  $p = 0$ , the above method yields the typical single-step GN method with sensitivity calculation, useful in situations requiring fast estimations of the conductivity distribution map in larger numerical domains. Both the single-step Gauss-Newton (sensitivity approach) and back-projection methods were used to compare the estimation performance obtained by the proposed non-linear method, that is, the resolution of the traditional 2D algebraic system for the GN method with TV regularization, as part of the **Results** section.

## References

1. Martins, T. C. *et al.* A review of electrical impedance tomography in lung applications: Theory and algorithms for absolute images. *Annu. Rev. Control.* **40**, 442–471, DOI: <https://doi.org/10.1016/j.arcontrol.2019.05.002> (2019).
2. Bluth, T. *et al.* Measurement of relative lung perfusion with electrical impedance and positron emission tomography: an experimental comparative study. *Br. J. Anaesth.* **123**, 246–254, DOI: <https://doi.org/10.1016/j.bja.2019.04.056> (2019).
3. Bayford, R. H. Bioimpedance tomography (electrical impedance tomography). *Annu. Rev. Biomed. Eng.* **8**, 63–91, DOI: <https://doi.org/10.1146/annurev.bioeng.8.061505.095716> (2006).

- 322 4. Huerta-Franco, M. R., Vargas-Luna, M., Montes-Frausto, J. B., Flores-Hernandez, C. & Morales-Mata, I. Electrical  
323 bioimpedance and other techniques for gastric emptying and motility evaluations. *World J. Gastrointest. Pathophysiol.* **3**,  
324 10–18, DOI: <https://doi.org/10.4291/wjgp.v3.i1.10> (2012).
- 325 5. Kimel-Naor, S., Abboud, S. & Arad, M. Parametric electrical impedance tomography for measuring bone mineral density  
326 in the pelvis using a computational model. *Med. Eng. & Phys.* **38**, 701–707, DOI: <https://doi.org/10.1016/j.medengphy.2016.04.013> (2016).
- 328 6. Fan, W., Wang, H., Yang, C. & Ma, S. Time series of eit measurements and images during lung ventilation based on  
329 principal component analysis. *Transactions Tianjin Univ.* **16**, 366–372, DOI: <https://doi.org/10.1007/s12209-010-1455-6>  
330 (2010).
- 331 7. Zhu, D., McEwan, A. & Eiber, C. Microelectrode array electrical impedance tomography for fast functional imaging in the  
332 thalamus. *NeuroImage* **198**, 44–52, DOI: <https://doi.org/10.1016/j.neuroimage.2019.05.023> (2019).
- 333 8. Yang, S., Strauss, T., Kupis, S. & Khan, T. Comparison of electrical impedance tomography and intracranial pressure  
334 during dehydration treatment of cerebral edema. *NeuroImage: Clin.* **23**, DOI: <https://doi.org/10.1016/j.nicl.2019.101909>  
335 (2019).
- 336 9. Leonhardt, S. *et al.* Electric impedance tomography for monitoring volume and size of the urinary bladder. *Biomed Tech*  
337 (*Berl.*) **56**, 301–307, DOI: <https://doi.org/10.1515/BMT.2011.022> (2011).
- 338 10. Dunne, E. *et al.* Supervised learning classifiers for electrical impedance-based bladder state detection. *Sci. Reports* **8**, 1–12,  
339 DOI: <https://doi.org/10.1038/s41598-018-23786-5> (2018).
- 340 11. Leonhauser, D. *et al.* Evaluation of electrical impedance tomography for determination of urinary bladder volume:  
341 comparison with standard ultrasound methods in healthy volunteers. *BioMedical Eng. OnLine* **17**, 1–13, DOI: <https://doi.org/10.1186/s12938-018-0526-0> (2018).
- 343 12. Prasad, S. N., Houserova, D. & Campbell, J. Breast imaging using 3d electrical impedance tomography. *Biomed Pap Med*  
344 *Fac Univ Palacky Olomouc Czech Repub* **152**, 151–154, DOI: <https://doi.org/10.5507/bp.2008.024> (2008).
- 345 13. Holder, D. Electrical impedance tomography. methods, history and applications – 1st ed. *CRC Press.* (2004).
- 346 14. Vogel, C. R. Computational methods for inverse problems. *SIAM Front. Appl. Math.* (2002).
- 347 15. Donatelli, M. & Serra-Capizzano, S. Computational methods for inverse problems in imaging. *Springer INdAM Ser.*  
348 (2019).
- 349 16. Santosa, F. & Vogelius, M. A backprojection algorithm for electrical impedance imaging. *SIAM J. on Appl. Math.* **50**,  
350 216–243, DOI: <https://doi.org/10.1137/0150014> (1990).
- 351 17. Schlebusch, T., Nienke, S., Leonhardt, S. & Walter, M. Bladder volume estimation from electrical impedance tomography.  
352 *Annu. Int Conf IEEE Eng Med Biol Soc* **35**, 1813–1823, DOI: <https://doi.org/10.1109/EMBC.2013.6611029> (2014).
- 353 18. Ahmad, S., Strauss, T., Kupis, S. & Khan, T. Comparison of statistical inversion with iteratively regularized gauss  
354 newton method for image reconstruction in electrical impedance tomography. *Appl. Math. Comput.* **358**, 438–448, DOI:  
355 <https://doi.org/10.1016/j.amc.2019.03.063> (2019).
- 356 19. Ma, Y. *et al.* A new modular semi-parallel eit system for medical application. *Biomed. Signal Process. Control.* **39**,  
357 416–423, DOI: <https://doi.org/10.1016/j.bspc.2017.08.001> (2018).
- 358 20. Borsic, A., Graham, B. M., Adler, A. & Lionheart, W. R. In vivo impedance imaging with total variation regularization.  
359 *IEEE Transactions on Med. Imaging* **29**, 44–54, DOI: <https://doi.org/10.1109/TMI.2009.2022540> (2010).
- 360 21. Zhou, Z. *et al.* Comparison of total variation algorithm for electrical impedance tomography. *Physiol. Meas.* **36**, 1193–1209,  
361 DOI: <https://doi.org/10.1088/0967-3334/36/6/1193> (2015).
- 362 22. Rosa, B. M. G. & Yang, G.-Z. Bladder volume monitoring using electrical impedance tomography with simultaneous  
363 multi-tone tissue stimulation and dft-based impedance calculation inside an fpga. *IEEE Transactions on Biomed. Circuits*  
364 *Syst.* **14**, 775–786, DOI: <https://doi.org/10.1109/TBCAS.2020.3008831> (2020).
- 365 23. Liu, S., Jia, J., Zhang, Y. D. & Yang, Y. Image reconstruction in electrical impedance tomography based on structure-aware  
366 sparse bayesian learning. *IEEE Transactions on Med. Imaging* **37**, 2090–2102, DOI: <https://doi.org/10.1109/TMI.2018.2816739> (2018).
- 368 24. Yang, G.-Z. Implantable sensors and systems: From theory to practice. *Springer Int. Publ. AG* (2018).

- 369 25. Gil, B., Anastasova, S. & Yang, G.-Z. A smart wireless ear-worn device for cardiovascular and sweat parameter monitoring  
370 during physical exercise: Design and performance results. *Sensors* **19**, 1–17, DOI: <https://doi.org/10.3390/s19071616>  
371 (2019).
- 372 26. Clemens, M. & Weiland, T. Discrete electromagnetism with the finite integration technique. *Prog. In Electromagn. Res.*  
373 **32**, 65–87, DOI: <https://doi.org/10.2528/PIER00080103> (2001).
- 374 27. Soleimani, M. Computational aspects of low frequency electrical and electromagnetic tomography: A review study. *Int. J.*  
375 *Numer. Analysis Model.* **5**, 407–440 (2008).
- 376 28. Grimmes, S. & Martinsen, O. Bioimpedance and bioelectricity basics. *Elsevier Ltd* **2nd Ed.** (2008).
- 377 29. Gabriel, C., Gabriel, S. & Corthout, E. The dielectric properties of biological tissues. literature survey. *Phys. Medicine &*  
378 *Biol.* **41**, 2231–2249, DOI: <https://doi.org/10.1088/0031-9155/41/11/001> (1996).
- 379 30. Chambolle, A. An algorithm for total variation minimization and applications. *J. Math. Imaging Vis. volume* **20**, 89–97,  
380 DOI: <https://doi.org/10.1023/B:JMIV.0000011325.36760.1e> (2004).
- 381 31. Bertsekas, D. P. Nonlinear programming. 2nd ed. *Athena Sci.* (1999).
- 382 32. Kelley, C. T. Iterative methods for optimization. *SIAM Front. Appl. Math.* (2002).
- 383 33. Bioucas-Dias, J. M., Figueiredo, M. A. T. & Oliveira, J. P. Total variation-based image deconvolution: a majorization-  
384 minimization approach. *IEEE Int. Conf. on Acoust. Speech Signal Process. Proc.* DOI: <https://doi.org/10.1109/ICASSP.2006.1660479> (2006).
- 385 34. Zhang, L. Image reconstruction algorithm for electrical impedance tomography using updated sensitivity approach. *Int. J.*  
386 *Adv. Pervasive Ubiquitous Comput.* **5**, DOI: <https://doi.org/10.4018/japuc.2013010103> (2013).
- 387 35. Mortarelli, J. R. A generalization of the gaselowitz relationship useful in impedance plethysmographic field calculations.  
388 *IEEE Trans Biomed Eng* **27**, 665–667, DOI: <https://doi.org/10.1109/TBME.1980.326677> (1980).
- 389 36. Brunner, P. *et al.* Reconstruction of the shape of conductivity spectra using differential multi-frequency magnetic induction  
390 tomography. *Physiol. Meas.* **27**, DOI: <https://doi.org/10.1088/0967-3334/27/5/S20> (2006).

## 392 Acknowledgements

393 The authors would like to thank to the Engineering and Physical Sciences Research Council (EPSRC) in the United Kingdom  
394 for the financial support under the project grants with references “EP/L014149/1” and “EP/R026092/1”.

## 395 Author contributions statement

396 B.M.G.R. designed the computational model, performed the experiments and wrote the paper. G.Z.Y. supervised the work and  
397 reviewed the paper.

## 398 Competing interests

399 The authors declare no competing interests.

## 400 Additional Information

401 Correspondence and requests for materials should be addressed to B.M.G.R.

# Figures

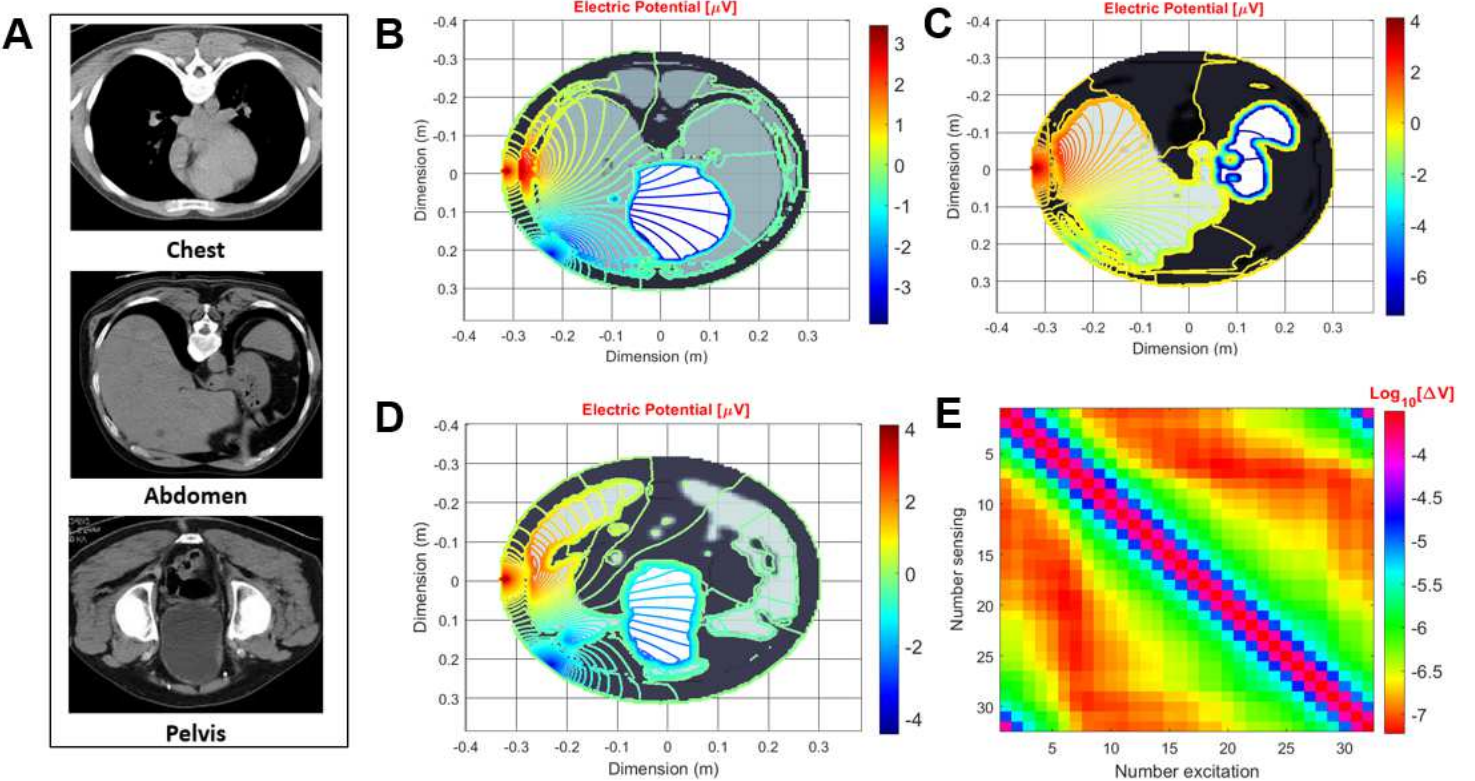


**Figure 1**

Resolution of the Forward Problem in EIT for medical images. A. MRI transverse slices from the chest, abdomen, and pelvic regions to be used as templates for the calculation of the electric potential distribution within these regions and imposed by off-body sources (electrodes). B. Potential distribution in the chest region when exciting from the left-side of the body. C. Potential distribution at the level of the liver (abdomen). D. Potential at the level of the urinary bladder (pelvic region). E. Potential difference (voltage) obtained at each electrode-sensing pair as a function of the excitation pair number (chest).

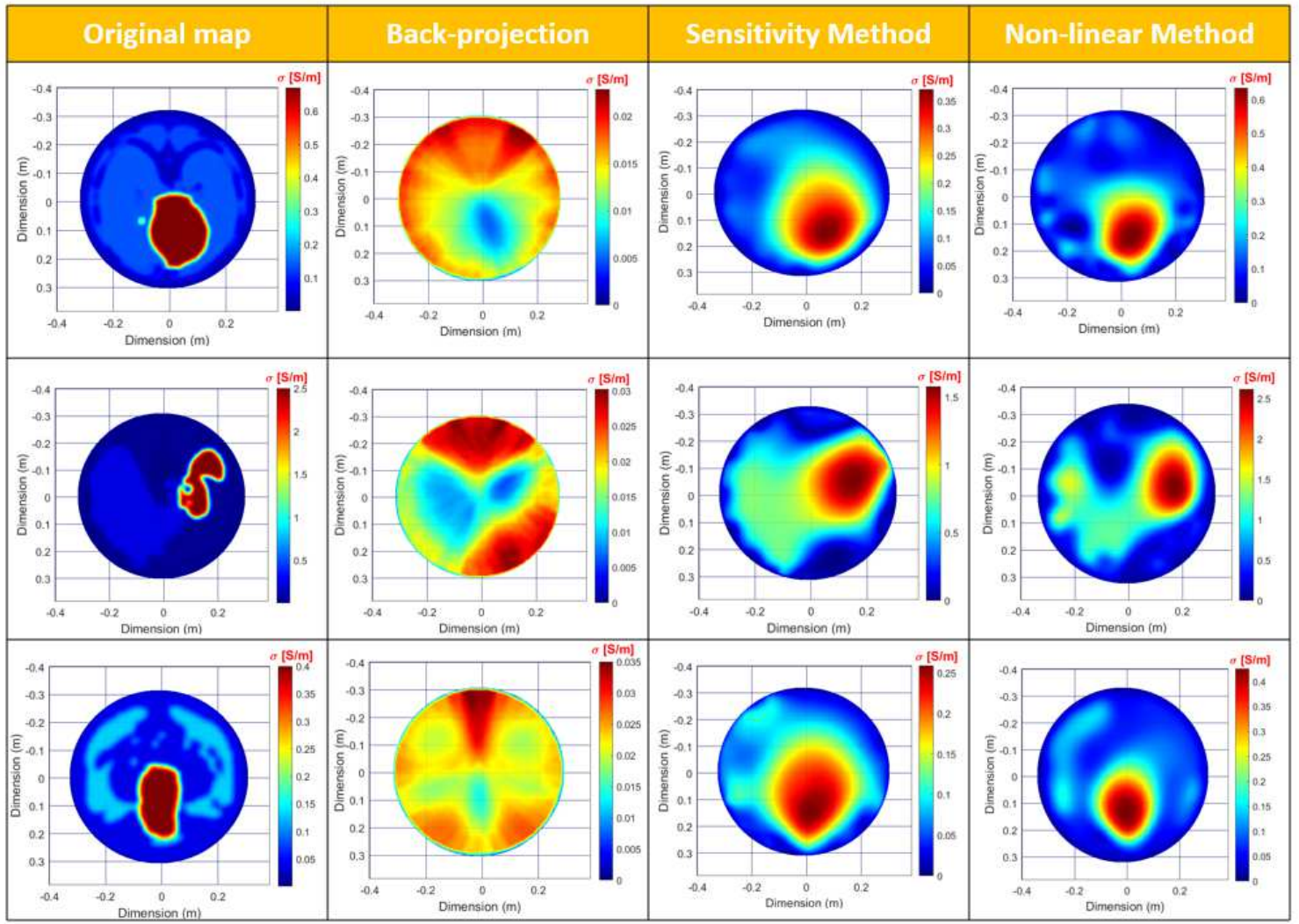


**Figure 2**

Conductivity reconstruction maps obtained by the three different methods (2D back-projection, GN with sensitivity and non-linear approaches) using 32 boundary electrodes, the adjacent electrode pair for current injection/measurement collection and SNR level of 30 dB for the collected vector of voltage potentials.

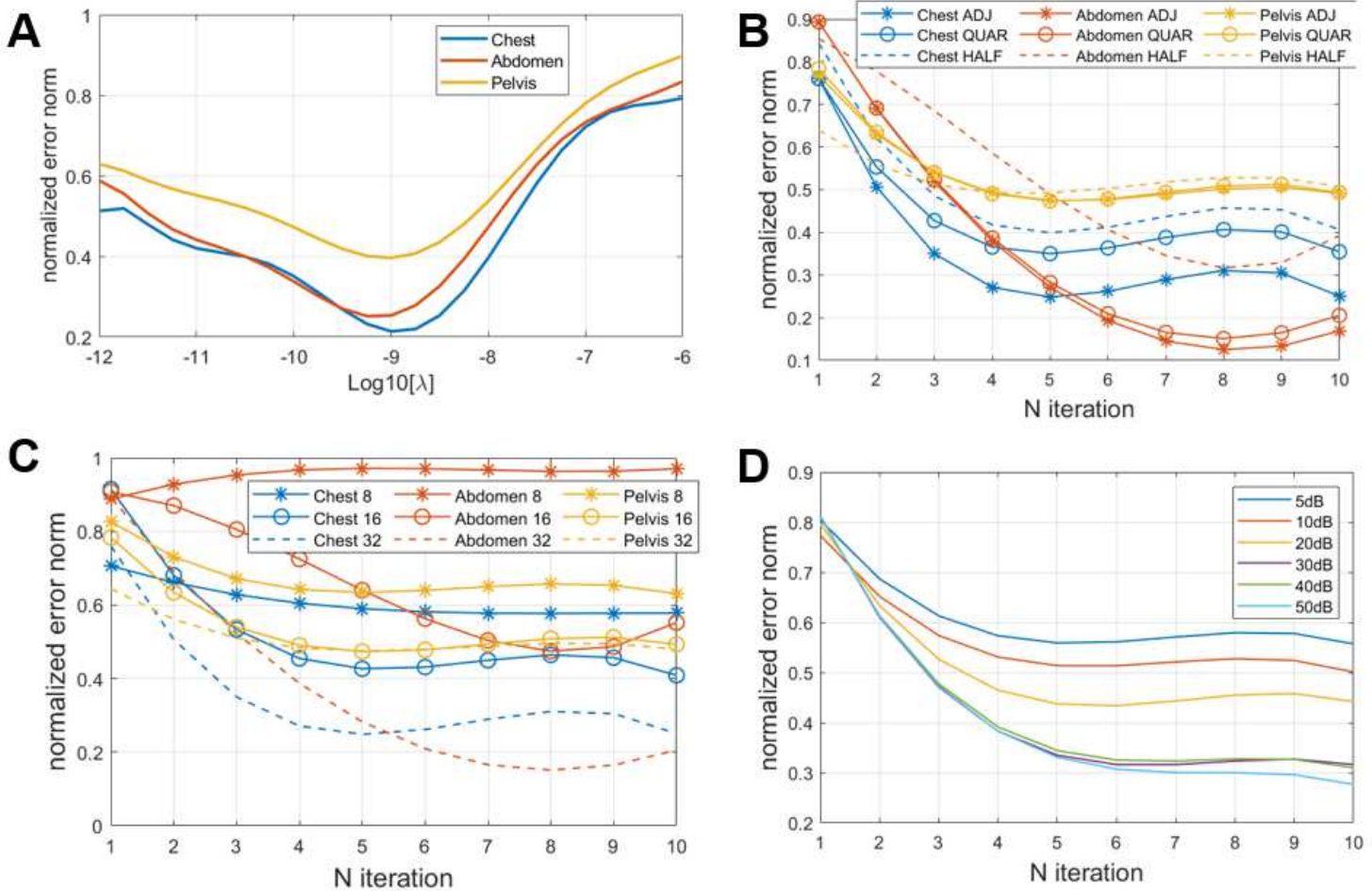


**Figure 3**

Performance metrics obtained for the chest, abdomen and pelvis phantoms, reconstructed by the proposed non-linear GN method. A. Evolution of the error norm as a function of the regularization parameter  $\lambda$  used in the reconstruction routine for the three phantoms (32 electrodes, adjacent electrode pair protocol, SNR level of 30 dB). B. Evolution of the normalized error norm as a function of the number of iterations for the phantoms with the same number of boundary electrodes (32), SNR level (30 dB) and different injection protocols (adjacent, quarter or half). C. Error norm evolution with iteration number for the phantoms with the same injection protocol (adjacent electrode-pair), SNR level (30 dB) and different number of boundary electrodes (8, 16 or 32). D. Error norm evolution along iterations calculated as an average value between the phantoms subjected to different SNR levels (adjacent protocol with 32 boundary electrodes).

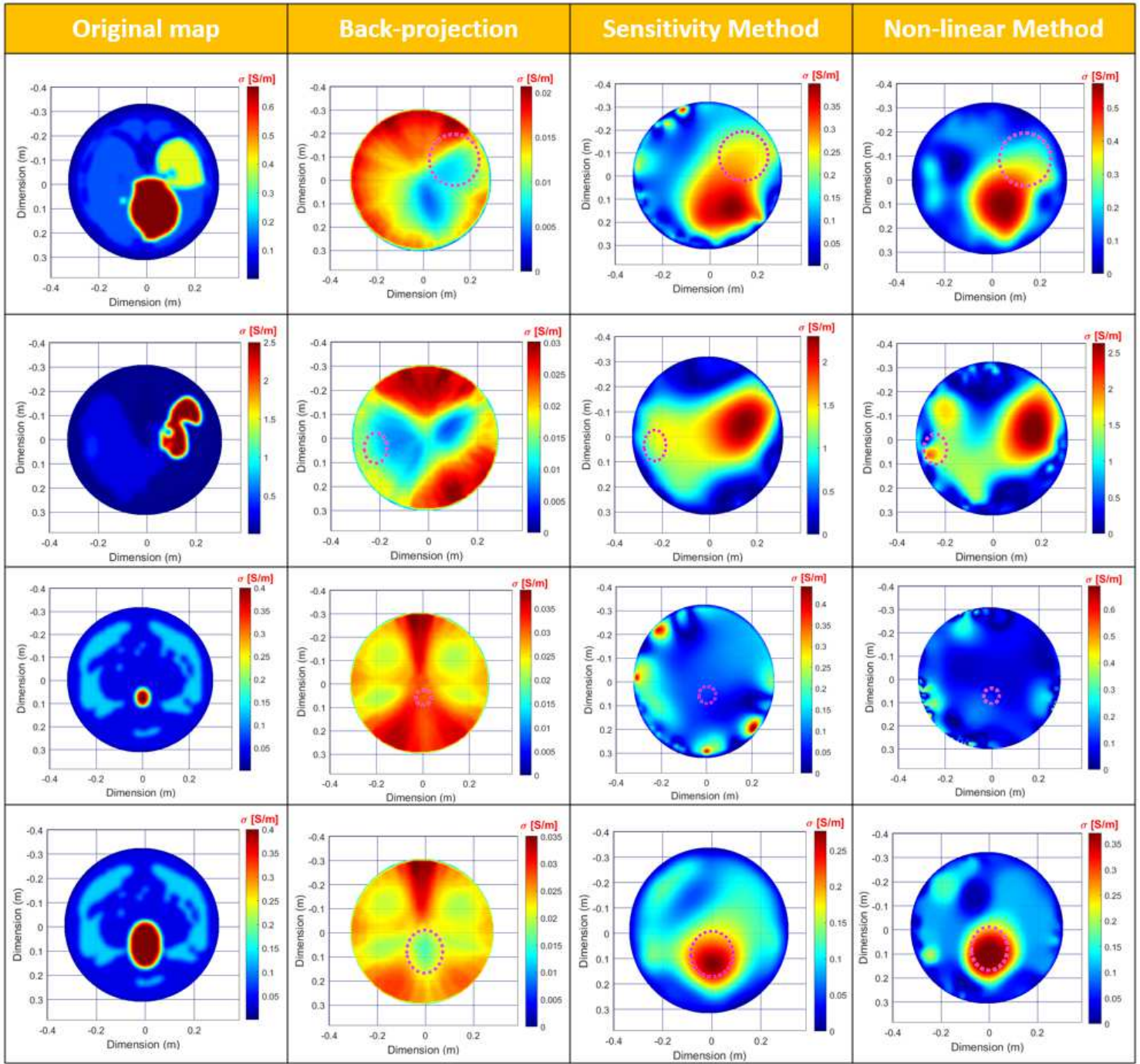


**Figure 4**

Conductivity reconstruction maps obtained for several tomographic slices located in the chest, abdomen and pelvis with affected areas (dashed circle) corresponding either to associated medical conditions (e.g., mass obstruction in the chest region and liver damage in the abdomen) or different volumes of enclosed conductivity (urine within the pelvis). These reconstructions were performed for the three numerical methods described within the manuscript (2D back-projection, GN with sensitivity and non-linear approaches) using a 32-electrode system with adjacent electrode pair protocol and SNR level of 30 dB.

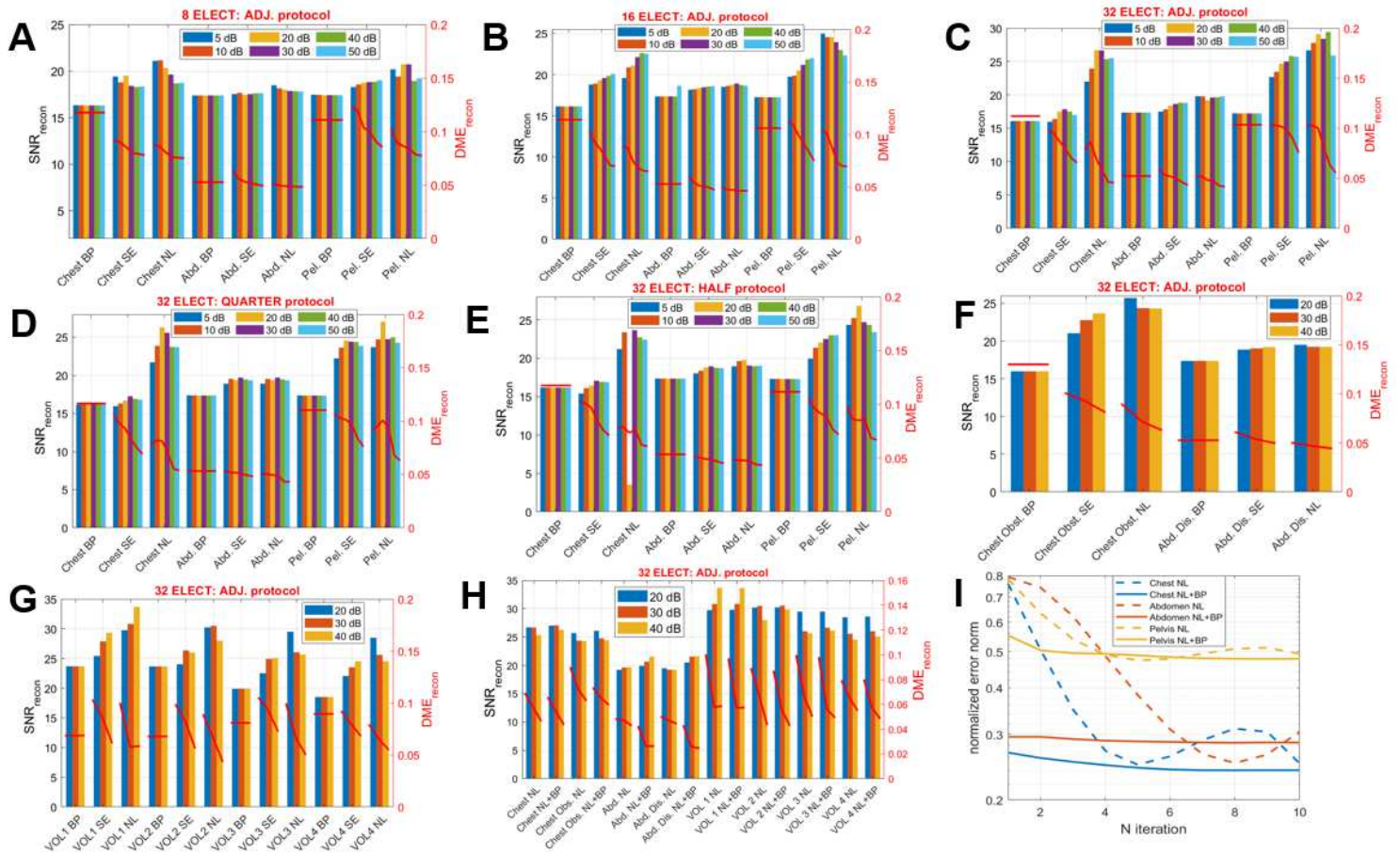


**Figure 5**

Performance metrics employed for quality assessment of the reconstruction maps for  $\sigma$  obtained by the numerical methods, under the influence of different initial conditions. A. Evolution of SNR<sub>recon</sub> (left) and DME<sub>recon</sub> (right) metrics for the chest, abdominal and pelvic phantoms using the 2D back-projection (BP), GN with sensitivity (SE) and non-linear (NL) approaches, in the condition of 8 boundary electrodes, adjacent electrode pair protocol and several SNR levels affecting the collected measurements. B. Same metrics evolution obtained when employing 16 boundary electrodes. C. Metrics evolution for a 32-electrode system. D. SNR<sub>recon</sub> and DME<sub>recon</sub> metrics for a 32-electrode system using the quarter injection/measurement protocol (separation of 8 electrodes). E. Identical metrics for the half injection/measurement protocol (separation of 16 electrodes in the 32-electrode system). F. Evolution of the performance metrics for the anatomical slices with associated medical conditions in the chest and abdominal phantoms (32-electrode system, adjacent electrode pair protocol and three SNR levels of added noise: 20, 30 and 40 dB). G. Same metrics for the condition of varying urinary bladder volume (4 discrete levels labelled from 1 to 4). H. Evolution of the performance metrics for all the tested phantoms, with initial blank conductivity distribution (NL) or estimate from the 2D back-projection method (NL+BP), used as the first iteration of the non-linear GN method. I. Evolution of the image error norm along the iterations of the proposed non-linear GN method for the chest, abdominal and pelvic phantoms (32-electrode system, adjacent electrode pair protocol, 20 dB SNR) with different initial conductivity map estimate: blank distribution (NL) and derived from back-projection (NL+BP).

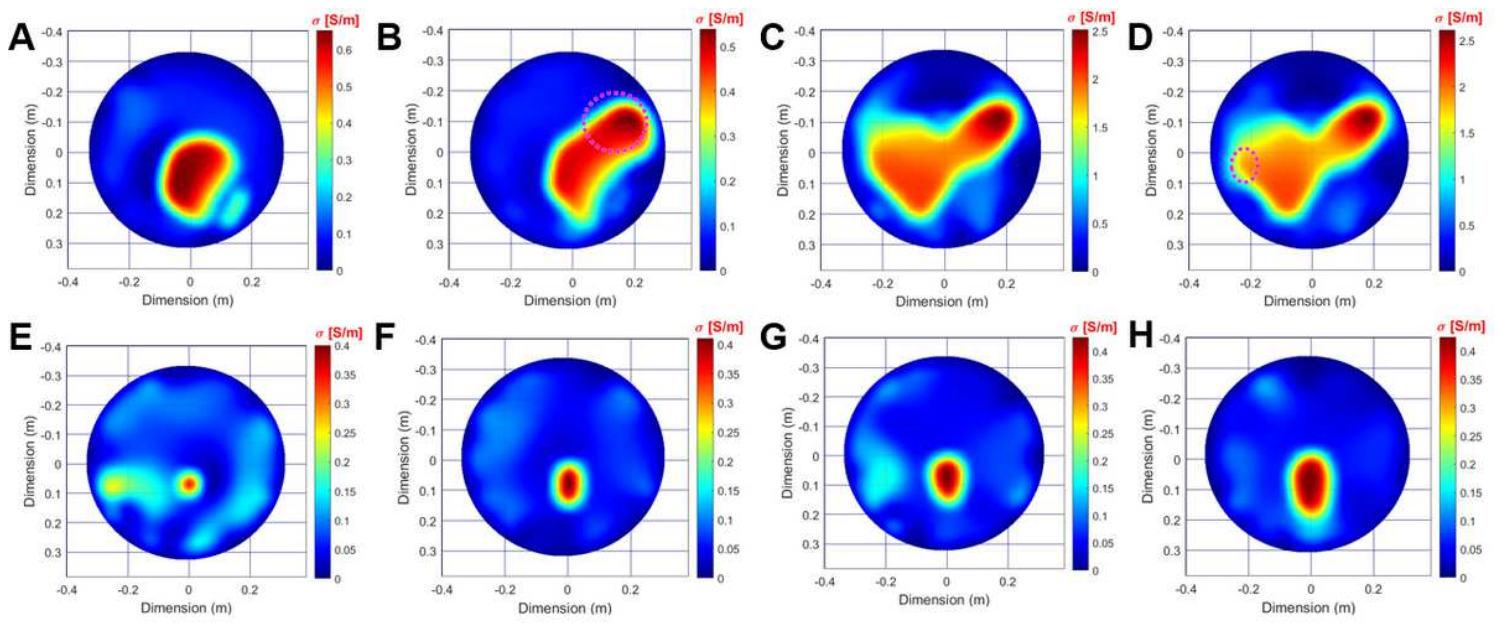


**Figure 6**

Conductivity reconstruction maps obtained for the proposed non-linear method with TV regularization and initial estimate obtained by the 2D back-projection method (32-electrode system, adjacent electrode pair protocol, SNR level of 20 dB). A. Chest phantom. B. Chest phantom with mass obstruction of the lung tissue encircled by the pink dashed circle. C. Abdominal phantom. D. Abdominal phantom with affected tissue damage inside the liver. E. Pelvic phantom with residual urinary bladder volume. F. Pelvic phantom with a lower intermediary volume contained inside the bladder walls. G. Pelvic phantom for a higher intermediary bladder volume. H. Pelvic phantom closer to the condition of full urinary bladder volume.

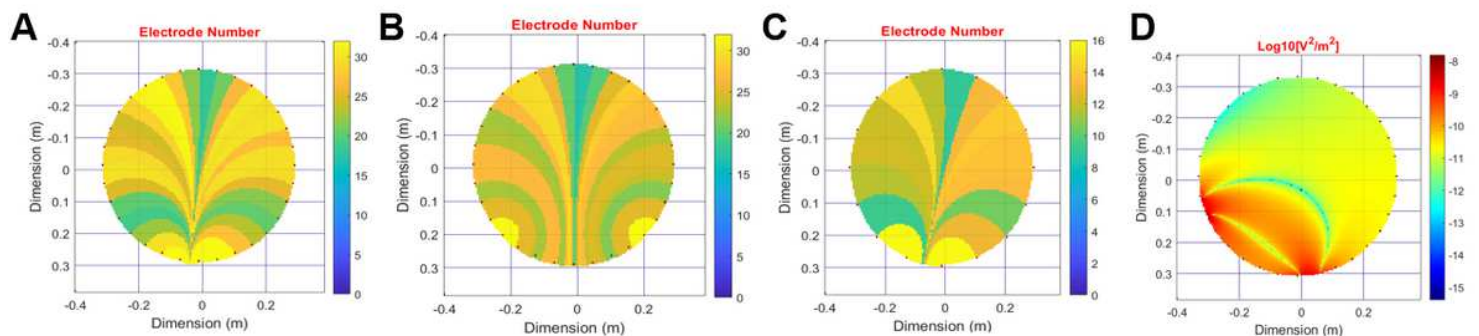


**Figure 7**

Intermediary maps obtained during the resolution of the Inverse Problem in EIT. A. Back-projection operator obtained using adjacent pair injection of current on a 32-electrode arrangement, with source and sink located in the bottom-most part of the phantom. B. Back-projection operator obtained for an 8-electrode spacing between source and sink on the same arrangement. C. Back-projection operator with adjacent pair injection of current on a 16-electrode arrangement. D. Sensitivity distribution for electrode pairs with different current injection and voltage detection numbers (32-electrode arrangement).